**Atmospheric
Measurement
Techniques
Discussions**

# Optical thickness and effective radius of Arctic boundary-layer clouds retrieved from airborne spectral and hyperspectral radiance measurements

E. Bierwirth[1], A. Ehrlich[1], M. Wendisch[1], J.-F. Gayet[2], C. Gourbeyre[2], R. Dupuy[2], A. Herber[3], R. Neuber[4], and A. Lampert[4,*]

[1]University of Leipzig, Institute for Meteorology, Leipzig, Germany
[2]Université Blaise Pascal, Laboratoire de Météorologie Physique, Aubière, France
[3]Alfred Wegener Institute for Polar and Marine Research, Bremerhaven, Germany
[4]Alfred Wegener Institute for Polar and Marine Research, Potsdam, Germany
[*]now at: Institute of Aerospace Systems, TU Braunschweig, Germany

Correspondence to: E. Bierwirth (eike.bierwirth@uni-leipzig.de)

**AMTD**

5, 7753–7781, 2012

**Optical thickness and effective radius of Arctic clouds**

E. Bierwirth et al.

Title Page

| Abstract | Introduction |
| Conclusions | References |
| Tables | Figures |

|◄ | ►|
◄ | ►

Back | Close

Full Screen / Esc

Printer-friendly Version

Interactive Discussion

**Abstract**

Arctic boundary-layer clouds in the vicinity of Svalbard (78° N, 15° E) were observed with airborne remote sensing and in situ methods. The cloud optical thickness and the droplet effective radius are retrieved from spectral radiance data in nadir and and from hyperspectral radiances in a 40° field of view. Two approaches are used for the spectral retrieval, combining the signal from either two or five wavelengths. Two wavelengths are found to be sufficient for an accurate retrieval of the cloud optical thickness, while the retrieval of droplet effective radius is more sensitive to the method applied. The comparison to in situ data cannot give a definite answer as to which method is better because of unavoidable time delays between the in situ measurements and the remote-sensing observations.

**1 Introduction**

The Arctic is strongly affected by global warming (Walsh et al., 2011), and clouds play an integral part in the ongoing changes (Wu and Lee, 2012). However, satellite observations are often obstructed by the low contrast between clouds and the surface covered by snow or sea ice (Krijger et al., 2011), and airborne or ground-based cloud observations are scarce, especially over the Arctic Ocean.

The understanding of Arctic clouds is crucial to predict their role in greenhouse warming (McBean et al., 2005). The Arctic heating trend was reported to continue in 2011 (Overland et al., 2011). The relationships between atmospheric conditions and the microphysical characteristics of mixed-phase clouds are key questions of cloud physics (Korolev and Isaac, 2006; de Boer et al., 2010; Seifert et al., 2010). Moreover, the microphysical characteristics of clouds (particle phase, size, concentration and shape) determine their radiative properties and, thus, their impact on the Earth's radiation budget (Curry et al., 1996; Ehrlich et al., 2008a). This is of particular interest in the Arctic where boundary-layer clouds greatly influence the surface radiation budget, as shown

E. Bierwirth et al.

by Shupe and Intrieri (2004) from ground-based remote-sensing observations, and climate change is particularly strong.

Verification of space-borne retrievals of cloud properties critically depends on independent airborne or ground-based measurements. Problems in retrievals arise from both instrument uncertainty and the assumptions made in the radiative transfer models used for the retrieval algorithms (Brest et al., 1997; Marshak et al., 2006). Thus, credible verification of remotely inferred cloud properties requires (i) direct comparison to in situ measurements; and (ii) comparison of spectral radiances simulated by radiative transfer models to measured quantities (Formenti and Wendisch, 2008; Barker et al., 2011).

For the purpose of improving the data base of the Arctic climate system, the SoRPIC (Solar Radiation and Phase Discrimination of Arctic Clouds) campaign was conducted in the Norwegian Arctic, including one of the first applications of an AisaEAGLE hyperspectral camera for cloud studies. SoRPIC was a collaboration of the Alfred Wegener Institute for Polar and Marine Research (AWI), the University of Leipzig (Germany), the Blaise Pascal University of Clermont-Ferrand (France), the Free University of Berlin (Germany), and the German Aerospace Center DLR. The measurement platform was the Polar-5 research aircraft (C-GAWI) of AWI, Bremerhaven (Germany). This Basler BT67 aircraft is a former DC-3 modernized by Basler Turbo Conversion Oshkosh (Wisconsin, USA) with modern avionics and navigation systems, and turbo prop engines required for the demands of polar research. It was put in service in 2007 (Herber et al., 2008). With an operational range of 1500 km, a maximum altitude of 7.5 km (24 000 feet), 15 kVA of electrical power, and a weight capacity of 2000 kg, the Polar-5 provides a reliable platform for the study of boundary-layer clouds in the Arctic. It is based out of Bremerhaven, Germany, and is presently operated by Kenn Borek Air Ltd., Calgary (Alberta, Canada).

In this manuscript, we follow the convention of defining hyperspectral data as imaging datasets with three dimensions (space, time, and wavelength) with contiguous spectral coverage, in contrast to multispectral where the spectral coverage is not contiguous.

The term spectral without prefix refers to non-imaging measurements that yield two-dimensional datasets (time and wavelength).

## 2  Measurements

During the SoRPIC campaign which was held in Svalbard (Arctic Norway) between
30 April and 20 May 2010, a total of 13 research flights were conducted with the Polar-5 aircraft over the Greenland, Norwegian, and Barents Seas.

The aircraft was equipped with a combination of remote-sensing and cloud-particle in situ instruments, listed in Table 1. Parts of the instrumentation are introduced in a recent book by Wendisch and Brenguier (2013). The remote-sensing equipment for this study included one active (the Airborne Mobile Aerosol Lidar AMALi; Stachlewska et al., 2010) and three passive systems (the Spectral Modular Airborne Radiation Measurement System (SMART-Albedometer); AisaEAGLE; Sun photometer). The hyperspectral imaging camera (AisaEAGLE, manufacturer: Specim Spectral Imaging Ltd., Oulu, Finland) was mounted in a tail-pod to measure upwelling radiances $I^{\uparrow}_{\lambda,\mathrm{E}}(t,y)$ as a function of wavelength $\lambda$, time $t$, and cross-track distance $y$ (subscript E for AisaEAGLE). The AisaEAGLE covers the spectral range from 403 nm to 966 nm in 240 channels, with a resolution (full width at half maximum) of 2–3 nm. The cross-track field of view was 40° wide, divided into 512 spatial pixels (1024 photo diodes with double binning). A dark measurement for correction of the thermal photo-current in the detector was performed every five minutes. An exposure time of 10 ms was used.

During all flights, the upwelling radiance $I^{\uparrow}_{\lambda,\mathrm{S}}(t,y_{\mathrm{n}})$ from the nadir point $y_{\mathrm{n}}$ was measured by the SMART-Albedometer (subscript S), which also measured spectral downwelling and upwelling irradiances, $F^{\downarrow}_{\lambda}(t)$ and $F^{\uparrow}_{\lambda}(t)$. The upwelling radiance reflected by the cloud is detected by an optical inlet with a field of view (FOV) of 1.5°; the irradiance by integrating spheres (Crowther, 1997). The collected photons are guided by fibre optics to grating spectrometers (manufactured by Zeiss, Jena/Germany; Bierwirth et al.,

2009) with 1280 channels for wavelengths from 350 to 2100 nm. An exposure time of 500 ms was used.

The viewing geometry for AisaEAGLE and SMART-Albedometer radiances is visualized in Fig. 1.

Both the AisaEAGLE and the SMART-Albedometer have an own Inertial Navigation System (INS) that records the aircraft attitude (roll, pitch, and heading angles). Using these attitude data, the optical inlets of the SMART-Albedometer are actively horizontally stabilised to correct for changes of the aircraft attitude of up to 6° with an accuracy of 0.2° (Wendisch et al., 2001). The AisaEAGLE is fixed to the fuselage, so the real-time attitude angles have to be taken into account in data analysis.

The AisaEAGLE and the SMART-Albedometer were calibrated in the laboratory with a NIST-traceable standard bulb for irradiances and with a NIST-traceable integrating sphere for radiances. The calibration stability during the campaign was monitored with a portable integrating sphere, and was better than 3 %. The radiometric uncertainty is given as 8 % for the AisaEAGLE and 9 % for the SMART-Albedometer radiance. The radiometric calibration of AisaEAGLE has been verified by comparing the upwelling radiances with that of the well-established SMART-Albedometer (compare Ehrlich et al., 2012). Using the INS attitude records, the AisaEAGLE pixels that are located in the field of view of the SMART-Albedometer's radiance sensor are identified for each time step. In this paper, such pixels are referred to as ES (the overlap is shown in Fig. 1). The mean value of all ES pixels is used for comparing AisaEAGLE and SMART-Albedometer radiance data, as in Fig. 2 for a wavelength of 870 nm. The linear correlation coefficient in Fig. 2 is 0.97; the differences can be attributed not only to the measurement uncertainty but also to the different time resolution (1–2 Hz for the SMART-Albedometer, 35 Hz for the AisaEAGLE).

The cloud-top altitude was determined from the backscatter signal of AMALi with an altitude resolution of 7.5 m. The in situ instrumentation includes the Cloud Particle Imager, CPI (Lawson et al., 1998), the Forward Scattering Spectrometer Probe, FSSP–100 (Dye and Baumgardner, 1984), and a polar nephelometer (Gayet et al., 1997).

# 3 Meteorological situation on 17 May

On 17 May 2010, a warm front approached Svalbard from Scandinavia, with unusually high temperatures up to 14 °C (Fig. 3). The warm, dry air (50 % relative humidity) was advected onto a ridge of about 0 °C which remained under an inversion at the ocean
surface. As observed by AMALi and the drop sondes (Fig. 4), both the inversion and the cloud top increased in altitude toward north. The maximum temperatures ranged from 14 °C at 800 m (74.5° N) to 8 °C at 1200 m altitude (75.9° N). A cloud layer formed in the inversion. On the aircraft, we observed that these clouds had a foggy appearance and reached down to the ocean surface. This is supported by the Bjørnøya sounding
(50 km west of the southern end of the flight track) that reports continuous saturation up to 975 hPa (Dietzsch, 2010). The Cloud Particle Imager was not operational on this flight. An additional higher cloud layer at 1500 m was observed to the north of the warm airmass, and is excluded from the following discussions.

The aircraft flew at 3100 m altitude almost parallel to the temperature gradient
(Fig. 3). Six drop sondes were launched; their data can be trusted only below 2900 m after their adjustment to ambient conditions. AMALi could detect only the cloud top due to saturation.

# 4 Retrieval of cloud properties from spectral radiance

The cloud properties are retrieved from the spectral and hyperspectral radiance mea-
surements aboard the Polar 5 aircraft. The measured data are checked against look-up tables (LUT) of simulated radiances. These look-up tables are produced with the radiative transfer package libRadtran (Mayer and Kylling, 2005). The radiative transfer calculations are initialised with environmental parameters from the SoRPIC campaign, including Sun/aircraft geometry, aerosol optical thickness from the Sun photometer,
cloud-top height from the AMALi lidar, and meteorological profiles from drop sondes released from the aircraft. The look-up tables then contain the possible values for the

spectral upward radiance in dependence on optical thickness $\tau$ and droplet effective radius $r_{eff}$ of a plane-parallel cloud, from which the most likely combination is obtained by interpolation of the measured radiance into the simulated radiance grid.

Two approaches have been followed to retrieve the cloud optical properties (optical thickness, effective radius) from spectral nadir radiance measurements by the SMART-Albedometer. First, the two-wavelength approach (2WL) presented by Nakajima and King (1990) is used with the radiance at 515 nm and 1625 nm. The grid of pre-calculated radiances $I_{LUT}$ is interpolated to the actual measured radiance $I_{meas}$ at these wavelengths. Second, a five-wavelength (5WL) residual approach presented by Coddington et al. (2010) is followed. The same look-up tables are used, but analysed at five wavelengths of 515, 745, 870, 1015, 1240, and 1625 nm in terms of the residuum $\zeta^2$:

$$\zeta^2 = \sum_{i=1}^{5} \left[ (5-i)^2 \cdot (I_{i,\text{meas}} - I_{i,\text{LUT}})^2 + (i-1)^2 \cdot \left( \frac{I_{i,\text{meas}}}{I_{0,\text{meas}}} - \frac{I_{i,\text{LUT}}}{I_{0,\text{LUT}}} \right)^2 \right], \tag{1}$$

where the index $i$ runs over the five wavelengths in increasing order. The weighting factors in Eq. (1) reflect the wavelength dependence of the radiance sensitivity to optical thickness (left term) and effective radius (right term). Each of the five wavelengths represents a different order of magnitude of the bulk absorption coefficient of liquid water and, adding the dependence on droplet size, different ranges of single-scattering albedo (Coddington et al., 2010, Fig. 2). For any given flight geometry, $\zeta^2$ is calculated for all elements of the corresponding look-up table, and the minimum indicates the most likely values of $r_{eff}$ and $\tau$. In order to propagate the reflectance measurement uncertainty into the retrieved quantity, both retrievals are repeated for the upper and the lower end of the radiance uncertainty range.

The retrieval results are shown in Fig. 5 for optical thickness $\tau_S$ and in Fig. 6 for the effective radius $r_{eff}^S$. In the case of optical thickness, the uncertainty (propagated from the reflectance measurement into $\tau_S$ space) behaves similarly for both retrieval approaches. As the difference between the two retrieval approaches lies within that

uncertainty, we conclude that either approach can be used to retrieve the optical thickness, and the inclusion of additional wavelengths does not provide additional information.

The retrieval of $r_{eff}^S$ is more differentiated. The uncertainties for both approaches differ significantly, with 5WL yielding lower uncertainties (less than 1 μm) than 2WL (1–2 μm). With values between 0 and 4 μm, the difference in $r_{eff}^S$ between 5WL and 2WL is close to and sometimes exceeds the retrievals' uncertainties. The additional wavelengths increase the retrieval sensitivity of the effective radius. The FSSP data (shown as red line in Fig. 6) are close to the retrieved value in the southern section of the flight, and deviates more strongly from the retrieval starting at and north of 75° N. There are two reasons for this: The time difference between in situ observations and remote sensing is smaller in the south, where the aircraft descended from the latter to the former; and south of 75° N, the in situ observations occurred near the cloud top, while at more northern latitudes the cloud top grew higher and the in situ observations came from a location deeper inside the cloud.

The retrieved $r_{eff}^S$ for 2WL and 5WL are compiled in Fig. 7 in form of two histograms, one for the flight section north of 75° N and one for the section south of 75° N. It shows that 2WL and 5WL yield similar distributions of $r_{eff}$ for the northern section, and both deviate equally from the in situ observations that occurred deeper in the cloud. On the other hand, 2WL and 5WL do not agree for the southern flight section, with the distribution from the FSSP observations near cloud top lie between the both. The 5WL retrieval reports a larger amount of large droplets, while 2WL prefers lower values. Judging by the lower retrieval uncertainty of 5WL, the larger values would seem more realistic; however, the deviation from the in situ distribution is beyond the FSSP uncertainty of 1 μm. Therefore it is impossible to validate neither 2WL nor 5WL with independent measurements, with the time delay between remote sensing and in situ observations being the most likely source of uncertainty.

# 5   Retrieval of cloud properties from hyperspectral radiance

The retrieval of the cloud properties from the hyperspectral radiances uses the same principles as for the spectral radiance. The benefit of the hyperspectral data is that they include off-track pixels, adding another dimension not only to the measured data but also to the look-up tables (viewing angle). However, the AisaEAGLE does not cover wavelengths longer than 1000 nm. Therefore, the effective radius cannot be retrieved for the off-track pixels of the AisaEAGLE because wavelengths shorter than 1000 nm are sensitive to the optical thickness only. In the following, the cloud optical thickness $\tau_E$ is retrieved from the 870 nm radiances for each pixel in the field of view of the AisaEA-GLE. For this purpose, the retrieval grid by Nakajima and King (1990) was constrained to a fixed value of the effective radius, $r_{\text{eff}}^{\text{fix}}$. This value is taken from other measurements on the same flight. As there are several options to choose the constraint of the effective radius, we first tested the sensitivity of the retrieval to the various available values.

## 5.1   Influence of effective radius

As we have no information about the effective radius in the off-track pixels, we make a basic assumption in the choice of the fixed value $r_{\text{eff}}^{\text{fix}}$: the cloud-particle statistics in this stratiform cloud layer is the same in $x$ (flight) and $y$ direction. Our first option for the effective radius is a moving average of the retrieval from the SMART-Albedometer, $r_{\text{eff}}^{\text{fix}}(t) = r_{\text{eff}}^{(1)} := \left\langle r_{\text{eff}}^{S}(t - \Delta t, t + \Delta t) \right\rangle$. Here, the averaging period $\Delta t$ is obtained as follows: First, the width $d$ of the observed strip of cloud is determined from the height $h$ between cloud top and the aircraft (from lidar) and the AisaEAGLE's field of view (40°). Then the nadir effective radii $r_{\text{eff}}^{S}(t)$ from the SMART-Albedometer are averaged over the time in which the radiance spot on the cloud top covered a distance $d$ that is determined from the aircraft speed as

$$d = v \cdot t + \left(2h \cdot \tan(\alpha_S/2)\right), \tag{2}$$

with $\alpha_S$ being the viewing angle of the radiance inlet and $v$ the aircraft speed (ignoring any cloud motion with the assumption $v \ll v_{cloud}$). The last term in Eq. (2) adds the radiance field of view behind and in front of the nadir point. Hence, the averaging time interval is $[t - \Delta t, t + \Delta t]$ with

$$2\Delta t = \left( d - 2h \cdot \tan \frac{\alpha_S}{2} \right) / v. \tag{3}$$

The other options for the choice of the effective radius include instantaneous and averaged values from remote sensing (S) or from in situ observations (index i). The complete list is this:

1. The moving average in nadir, $r_{eff}^{(1)} := \left\langle r_{eff}^{S}(t - \Delta t, t + \Delta t) \right\rangle$;

2. the current effective radius in nadir, $r_{eff}^{(2)}(t) := r_{eff}^{S}(t)$;

3. the mean effective radius of the entire flight leg, $r_{eff}^{(3)} := \left\langle r_{eff}^{S}(t) \right\rangle \; \forall \, t$;

4. the value measured by in situ instruments at the same location $x$, $r_{eff}^{(4)}(t) := r_{eff}^{i}(x^{i} = x^{S}(t))$, where $x^{i}$ is the aircraft location during the in situ measurements and $x^{S}$ during the remote-sensing leg;

5. the mean value of all in situ measurements, $r_{eff}^{(5)} := \left\langle r_{eff}^{i}(x^{i}) \right\rangle \; \forall \, x^{i}$.

All five options for $r_{eff}^{fix}$ are used as a constraint to derive the optical thickness for all off-track AisaEAGLE pixels. This results in a spread of the optical thickness $\tau_{ES}$ in the ES pixels of 0.3–0.4 units of optical thickness, which is less than the retrieval uncertainty.

The histograms of the entire field of optical thickness retrieved with the five different constraints of effective radius (Fig. 8) shows that the choice matters only when the optical thickness is less than 8. One choice, $r_{eff}^{(4)}$, leads to a significantly lower retrieval of

those low optical thicknesses. This is because of the large time delay between remote sensing and in situ observations. Thin cloud parts are more likely to be changed by weak turbulence than thick stretches of cloud, rendering the local properties detected in situ less representative for the remote sensing at the same location but one hour earlier. We conclude that $r_{\text{eff}}^{(4)}$ is a poor choice, while the other options yield very similar results in the retrieval of the optical thickness.

## 5.2 Influence of atmospheric profile

The variation of the vertical structure of the atmosphere along the flight track has been recorded by a series of drop sondes. The major change occurred in the height of the cloud top, which increased from 200 m at the southern end of the flight track to 700 m at the northern end. In order to illustrate the potential influence of the atmospheric profile, the look-up tables for the 2WL retrieval were computed for four drop sonde profiles. Between one drop sonde and the next (time interval: 15 min), two sets of $\tau_{\text{ES}}$ differ by up to 0.2 (0.4 in peaks). The difference is greater when a more distant drop sonde is used; the two retrievals that assume the first and the last drop sonde, respectively, differ by up to one unit of optical thickness. In the following, however, we interpolate between look-up tables created for the different drop sondes in order to mitigate this source of uncertainty.

## 5.3 Retrieval results

The hyperspectral data from the AisaEAGLE produce a map of the retrieved cloud optical thickness. An example is shown in Fig. 10. This map has been drawn such that the aircraft nadir (marked with the red line) is always in the centre. The wavy edge of the map represents the rolling of the aircraft in flight. The ES pixels that are observed by the SMART-Albedometer radiance surround the nadir point and are delineated by the blue lines.

The following statistics of the cloud properties for 17 May are based on the retrieval that uses the current effective radius $r_{\text{eff}}^{(2)}(t)$ from the SMART-Albedometer. The look-up tables were calculated for a range of values of solar zenith angle, cloud-top height, and meteorological profiles, and were then interpolated to the current conditions of each measurement point. The resulting look-up table contained radiances only as a function of viewing angle and cloud optical thickness. The viewing angle is fixed for each pixel of the hyperspectral camera, and modified by the aircraft roll angle. So for each pixel, the radiance is a function of $\tau$, and the radiance measured by this pixel yields the retrieved $\tau$ value at this point. On the flight on 17 May, a total of $4 \times 10^7$ values were retrieved; see the histogram in Fig. 11. The histograms for the entire field of view and for the ES pixels do not differ significantly, which justifies the assumption that the cloud statistics are the same in flight direction and across (on the scale of the field of view). It can roughly be compared to the nadir values retrieved from the SMART-Albedometer radiance: While the AisaEAGLE has about 20 times more data points, the shape of the distribution is the same as for the nadir optical thickness of the SMART-Albedometer, with the exception of the bins for $\tau = 6$–$10$ that are more pronounced. Only the ES pixels can be directly compared to the simultaneous retrieval by the SMART-Albedometer in nadir (Fig. 12). As these mostly agree within the retrieval uncertainty, the differences in the histogram have to originate in slight off-track deviations in the horizontal distribution of the optical thickness, which nadir observations alone would not observe.

## 6 Conclusions

Both a two-wavelength (2WL) and a five-wavelength (5WL) approach have been applied to retrieve the cloud optical thickness and effective radius from the nadir radiances of the SMART-Albedometer. While the two approaches agree within uncertainty for the optical thickness, they differ in respect to effective radius: 5WL seems to be more sensitive to larger droplets (more than 10 μm radius) than 2WL. However, even with comprehensive instrumentation during the SoRPIC campaign that includes state-of-the-art

remote sensing and in situ instrumentation, it is impossible to give a definite answer to the question which of the two methods yields better results. The fundamental limitation is the time delay which cannot be avoided when remote sensing and in situ observations are performed on the same platform, but also the vertical position within the cloud.

5  Only with simultaneous collocated measurements above and inside the cloud (with two aircraft) can this limitation be overcome and can closure between the different methods be attempted.

Hyperspectral imaging was used to retrieve the cloud optical thickness in a 40° field of view across the flight track. This extends the application of the hyperspectral camera
10  AisaEAGLE to airborne cloud research, and shows the potential of this rapidly developing technology to this purpose. We found that the distribution of the cloud optical thickness derived from the hyperspectral data are not entirely equal to those derived from the nadir radiance. Hyperspectral observations are therefore a tool to improve cloud statistics in remote sensing.

15  With our current instrumentation, the hyperspectral retrieval is limited to the cloud optical thickness, because the AisaEAGLE does not cover the wavelengths required for a retrieval of the effective radius. However, compatible hyperspectral imagers for those wavelengths already exist and could be successfully applied to retrieve the effective radius additionally.

# References

Barker, H. W., Jerg, M. P., Wehr, T., Kato, S., Donovan, D. P., and Hogan, R. J.: A 3-D cloud construction algorithm for the EarthCARE satellite mission, Q. J. Roy. Meteor. Soc., 137, 1042–1058, 2011. 7755

Bierwirth, E., Wendisch, M., Ehrlich, A., Heese, B., Tesche, M., Althausen, D., Schladitz, A., Müller, D., Otto, S., Trautmann, T., Dinter, T., von Hoyningen-Huehne, W., and Kahn, R.: Spectral surface albedo over Morocco and its impact on radiative forcing of Saharan dust, Tellus B, 61, 252–269, 2009. 7756

Brest, C. L., Rossow, W. B., and Roiter, M. D.: Update of Radiance Calibrations for ISCC P., J. Atmos. Ocean. Technol., 14, 1091–1109, 1997. 7755

Coddington, O. M., Pilewskie, P., Redemann, J., Platnick, S., Russell, P. B., Schmidt, K. S., Gore, W. J., Livingston, J., Wind, G., and Vukicevic, T.: Examining the impact of overlying aerosols on the retrieval of cloud optical properties from passive remote sensing, J. Geophys. Res., 115, D10211, doi:10.1029/2009JD012829, 2010. 7759

Crowther, B.: The Design, Construction, and Calibration of a Spectral Diffuse/Global Irradiance Meter, Ph. D. thesis, University of Arizona, Tucson, USA, 1997. 7756

Curry, J. A., Rossow, W. B., Randall, D., and Schramm, J. M.: Overview of Arctic cloud and radiation characteristics, J. Climate, 9, 1731–1764, 1996. 7754

de Boer, G., Hashino, T., and Tripoli, G. J.: Ice nucleation through immersion freezing in mixed-phase stratiform clouds: Theory and numerical simulations, Atmos. Res., 96, 315–324, 2010. 7754

Dietzsch, F.: Charakaterisierung der synoptischen Situation während der Kampagne SORPIC April/Mai 2010, B. S. Thesis, University of Leipzig, Germany, 2010. 7758

Dye, J. E. and Baumgardner, D.: Evaluation of the forward scattering spectrometer probe. Part I: electronic and optical studies, J. Atmos. Ocean. Tech., 1, 329–344, 1984. 7757

Ehrlich, A., Wendisch, M., Bierwirth, E., Herber, A., and Schwarzenböck, A.: Ice crystal shape effects on solar radiative properties of arctic mixed-phase clouds – dependence on microphysical properties, Atmos. Res., 88, 266–276, 2008. 7754

Ehrlich, A., Bierwirth, E., Wendisch, M., Herber, A., and Gayet, J.-F.: Airborne hyperspectral observations of surface and cloud directional reflectivity using a commercial digital camera, Atmos. Chem. Phys., 12, 3493–3510, doi:10.5194/acp-12-3493-2012, 2012. 7757

**Optical thickness and effective radius of Arctic clouds**

E. Bierwirth et al.

Title Page

Abstract | Introduction

Conclusions | References

Tables | Figures

⏮ | ⏭

◀ | ▶

Back | Close

Full Screen / Esc

Printer-friendly Version

Interactive Discussion

Formenti, P. and Wendisch, M.: Combining upcoming satellite missions and aircraft activities, B. Am. Meteorol. Soc., 89, 385–388, 2008. 7755

Gayet, J. F., Crépel, O., Fournol, J. F., and Oshchepkov, S.: A new airborne polar Nephelometer for the measurements of optical and microphysical cloud properties. Part I: Theoretical design, Ann. Geophys., 15, 451–459, doi:10.1007/s00585-997-0451-1, 1997. 7757

Herber, A., Dethloff, K., Haas, C., Steinhage, D., Strapp, J. W., Bottenheim, J., McElroy, T., and Yamanouchi, T.: POLAR 5 – a new research aircraft for improved access to the Arctic, in: Extended Abstracts of the First International Symposium on the Arctic Research (ISAR–1), Miraikan, Japan, 4–6 November 2008, 54–57, 2008. 7755

Korolev, A. and Isaac, G. A.: Relative humidity in liquid, mixed-phase, and ice clouds, J. Atmos. Sci., 63, 2865–2880, doi:10.1175/JAS3784.1, 2006. 7754

Krijger, J. M., Tol, P., Istomina, L. G., Schlundt, C., Schrijver, H., and Aben, I.: Improved identification of clouds and ice/snow covered surfaces in SCIAMACHY observations, Atmos. Meas. Tech., 4, 2213–2224, doi:10.5194/amt-4-2213-2011, 2011. 7754

Lawson, R. P., Korolev, A. V., Cober, S. G., Huang, T., Strapp, J. W., and Isaac, G. A.: Improved measurements of the drop size distribution of a freezing drizzle event, Atmos. Res., 47–48, 181–191, 1998. 7757

Marshak, A., Platnick, S., Várnai, T., Wen, G., and Cahalan, R. F.: Impact of three-dimensional radiative effects on satellite retrievals of cloud droplet sizes, J. Geophys. Res., 111, D09207, doi:10.1029/2005JD006686, 2006. 7755

Mayer, B. and Kylling, A.: Technical note: the libRadtran software package for radiative transfer calculations – description and examples of use, Atmos. Chem. Phys., 5, 1855–1877, doi:10.5194/acp-5-1855-2005, 2005. 7758

McBean, G., Alekseev, G., Chen, D., Forland, E., Fyfe, J., Groisman, P. Y., King, R., Melling, H., Vose, R., and Whitfield, P. H.: Arctic Climate: Past and Present, in Arctic Climate Impact Assessment, edited by: Symon, C., Arris, L., and Heal, B., 21–60, Cambridge University Press, New York, NY, 2005. 7754

Nakajima, T. and King, M.: Determination of the optical thickness and effective particle radius of clouds from reflected solar radiation measurements. Part I: theory, J. Atmos. Sci., 47, 1878–1893, 1990. 7759, 7761

Overland, J., Bhatt, U., Key, J., Liu, Y., Walsh, J., and Wang, M.: Temperature and Clouds (in Arctic Report Card 2011), available at: http://www.arctic.noaa.gov/reportcard, last access: 11 July 2012. 7754

Title Page

Abstract | Introduction

Conclusions | References

Tables | Figures

|◄ | ►|

◄ | ►

Back | Close

Full Screen / Esc

Printer-friendly Version

Interactive Discussion

Pietsch, A.: Analyse der Messgenauigkeit von Temperatur- und Feuchteprofilen aus Flugzeug-, Radiosonden- und Dropsondenmessungen und Vergleich mit Simulationen des ECMWF-Modells für Fallbeispiele der SORPIC Messkampagne, B. S. Thesis, University of Leipzig, Germany, 2011.

5  Seifert, P., Ansmann, A., Mattis, I., Wandinger, U., Tesche, M., Engelmann, R., Müller, D., Pérez, C., and Haustein, K.: Saharan dust and heterogeneous ice formation: Eleven years of cloud observations at a Central European EARLINET site, J. Geophys. Res., 115, D20201, doi:10.1029/2009JD013222, 2010. 7754

Shupe, M. D. and Intrieri, J. M.: Cloud radiative forcing of the arctic surface: the influence of
10  cloud properties, surface albedo, and solar zenith angle, J. Climate., 17, 616–628, 2004. 7755

Stachlewska, I. S., Neuber, R., Lampert, A., Ritter, C., and Wehrle, G.: AMALi – the airborne mobile aerosol lidar for arctic research, Atmos. Chem. Phys., 10, 2947–2963, doi:10.5194/acp-10-2947-2010, 2010. 7756

15  Walsh, J. E., Overland, J. E., Groisman, P. Y., and Rudolf, B.: Ongoing climate change in the Arctic, AMBIO, 40, 6–16, doi:10.1007/s13280-011-0211-z, 2011. 7754

Wendisch, M. and Brenguier, J.-L. (Eds.): Airborne Measurements for Environmental Research: Methods and Instruments, Wiley-VCH Verlag GmbH & Co. KGaA, Weinheim, Germany, ISBN: 978-3-527-40996-9, in press, 2013. 7756

20  Wendisch, M., Müller, D., Schell, D., and Heintzenberg, J.: An airborne spectral albedometer with active horizontal stabilization, J. Atmos. Ocean. Tech., 18, 1856–1866, 2001. 7757

Wu, D. L. and Lee, J. N.: Arctic low cloud changes as observed by MISR and CALIOP: implication for the enhanced autumnal warming and sea ice loss, J. Geophys. Res., 117, D07107, doi:10.1029/2011JD017050, 2012. 7754

Discussion Paper | Discussion Paper | Discussion Paper | Discussion Paper

**Table 1.** Instrumentation during SoRPIC. Acronyms: AMALi, FSSP (Forward Scattering Spectrometer Probe), CPI (Cloud Particle Imager), AMSSP (Airborne Multi Spectral Sunphoto- and Polarimeter), AIMMS (Advanced Airborne MeasureMent Solutions).

| Instrument | Measured Quantity | Unit | Range |
|---|---|---|---|
| SMART-Albedometer | Radiance | $\mathrm{W\,m^{-2}\,nm^{-1}\,sr^{-1}}$ | $\lambda = 350\text{--}2100\,\mathrm{nm}$ |
| | Irradiance | $\mathrm{W\,m^{-2}\,nm^{-1}}$ | $\lambda = 350\text{--}2100\,\mathrm{nm}$ |
| AisaEAGLE | Radiance | $\mathrm{W\,m^{-2}\,nm^{-1}\,sr^{-1}}$ | $\lambda = 400\text{--}1000\,\mathrm{nm}$ |
| AMALi | Extinction Coefficient | $\mathrm{km^{-1}}$ | $\lambda = 355\,\mathrm{nm},\ 532\,\mathrm{nm}$ |
| | Cloud Top Height | m | $z = 0\text{--}3\,\mathrm{km}$ |
| FSSP–100 | Particle Number Concentration | $\mathrm{cm^{-3}\,\mu m^{-1}}$ | $d = 3\text{--}95\,\mu\mathrm{m}$ |
| | Effective Diameter | $\mu\mathrm{m}$ | |
| | Liquid Water Content | $\mathrm{g\,m^{-3}}$ | |
| | Extinction Coefficient | $\mathrm{km^{-1}}$ | |
| Polar Nephelometer | Scattering Phase Function | $\mathrm{W\,sr^{-1}}$ | $d = 3\text{--}1000\,\mu\mathrm{m}$ |
| | | | $\theta = 3.5\text{--}169^{\circ}$ |
| CPI | Particle Number Concentration | $\mathrm{l^{-1}\,\mu m^{-1}}$ | $\Delta x = 2.3\,\mu\mathrm{m}$ |
| | Effective Diameter | $\mu\mathrm{m}$ | |
| | Extinction Coefficient | $\mathrm{km^{-1}}$ | |
| | Ice Water Content | $\mathrm{g\,m^{-3}}$ | |
| CANON Camera | RGB Radiance | $\mathrm{W\,m^{-2}\,nm^{-1}\,sr^{-1}}$ | $\lambda = (446, 530, 591)\,\mathrm{nm}$ |
| Sun Photometer | Aerosol Optical Thickness | 1 | $\lambda = 367\text{--}1026\,\mathrm{nm}$ |
| Nevzorov Sonde | Liquid/Total Water Content | $\mathrm{g\,m^{-3}}$ | $0.003\text{--}3\,\mathrm{g\,m^{-3}}$ |
| AMSSP | Stokes Vector | $\mathrm{W\,m^{-2}\,nm^{-1}}$ | $\lambda = 350\text{--}1000\,\mathrm{nm}$ |
| AIMMS–20 | Pressure | hPa | |
| | Temperature | $^{\circ}\mathrm{C}$ | |
| | Relative Humidity | % | |
| | Wind Vector | $\mathrm{m\,s^{-1}}$ | |
| Drop Sondes | Pressure | hPa | |
| | Temperature | $^{\circ}\mathrm{C}$ | |
| | Relative Humidity | % | |

**Fig. 1.** Viewing geometry for radiances from the Polar-5 aircraft with the hyperspectral camera AisaEAGLE (black) and the SMART-Albedometer (blue). Typical dimensions in this study: distance aircraft–cloud $h = 2600$ m, aircraft speed $v = 70$ m s$^{-1}$, width of one AisaEAGLE pixel $y_E = 3.5$ m, length $x_E = y_E + v \cdot t_E = 4.2$ m with the exposure time $t_E = 10$ ms, width of instantaneous SMART-Albedometer field of view $y_S = 68$ m, length due to exposure time $t_S = 0.5$ s: $x_S = y_S + v \cdot t_S = 103$ m.
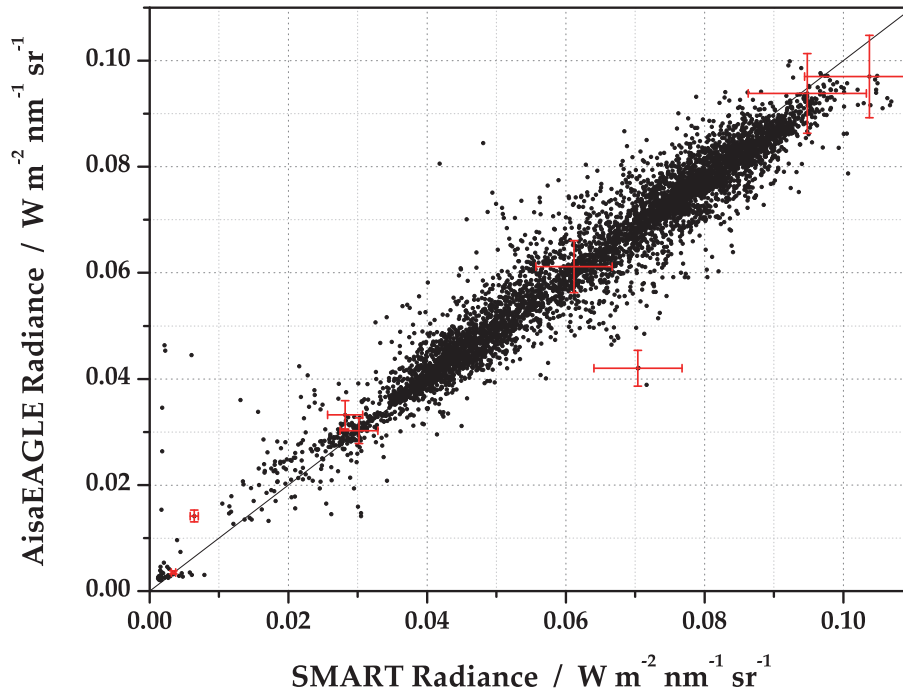
**Fig. 2.** Comparison of the 870 nm radiance from the SMART-Albedometer and from the SMART spot of the AisaEAGLE for the flight on 17 May 2010. The radiometric uncertainty (8 % for AisaEAGLE, 9 % for SMART-Albedometer) are marked with red crosses at exemplary wavelengths.
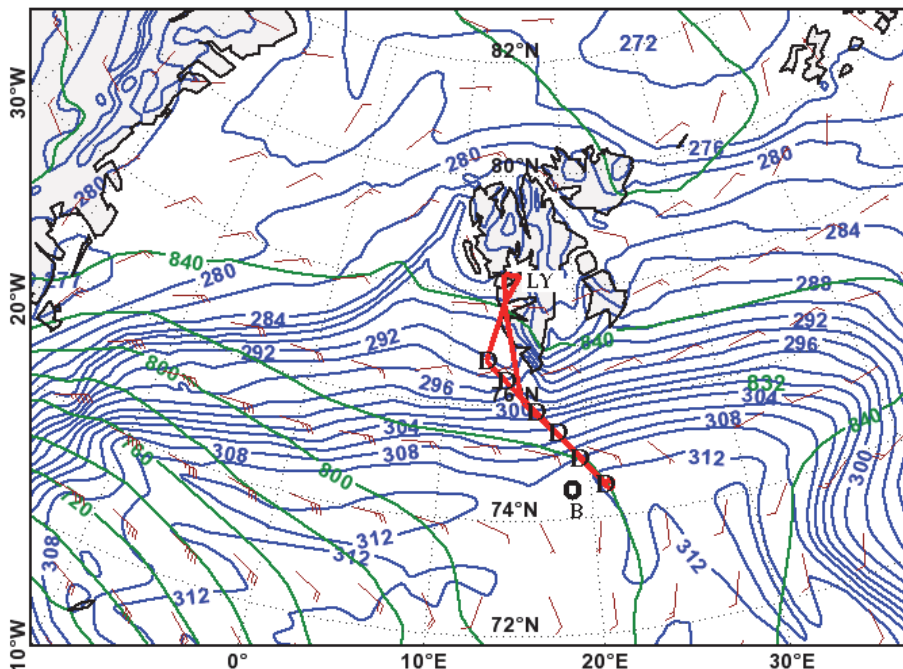
**Fig. 3.** ECMWF analysis chart (925 hPa, 12:00 UTC) and SoRPIC flight track on 17 May 2010, from Longyearbyen (LY) to 50 km east of Bjørnøya (B) and back. Dropsondes were launched at the D symbols. The contours are the geopotential height in m (green) and the equivalent potential temperature in K (blue).
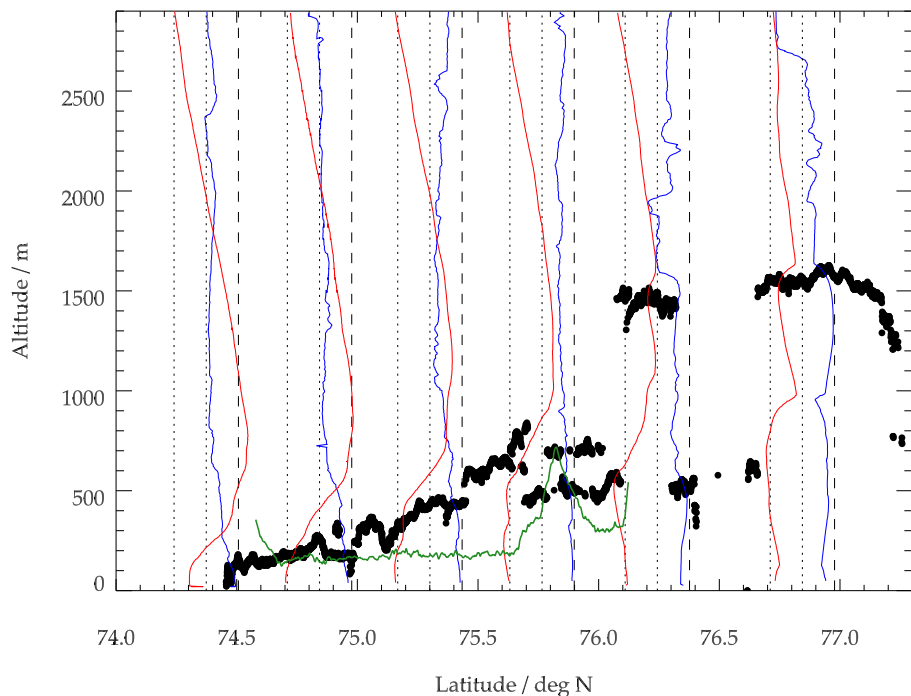
**Fig. 4.** Dropsonde profiles (red: temperature, blue: relative humidity) and lidar cloud-top altitude (black) for 17 March 2010. Each drop-sonde profile is marked with one dashed and two dotted lines; the dashed lines are placed at the times of launch, and also represent a temperature of 12 °C and 100 % RH. The central dotted lines show 6 °C and 50 %, the left dotted lines show 0 °C and 0 %. The green line represents the flight altitude during the in situ observations.

Full Screen / Esc

Printer-friendly Version

Interactive Discussion
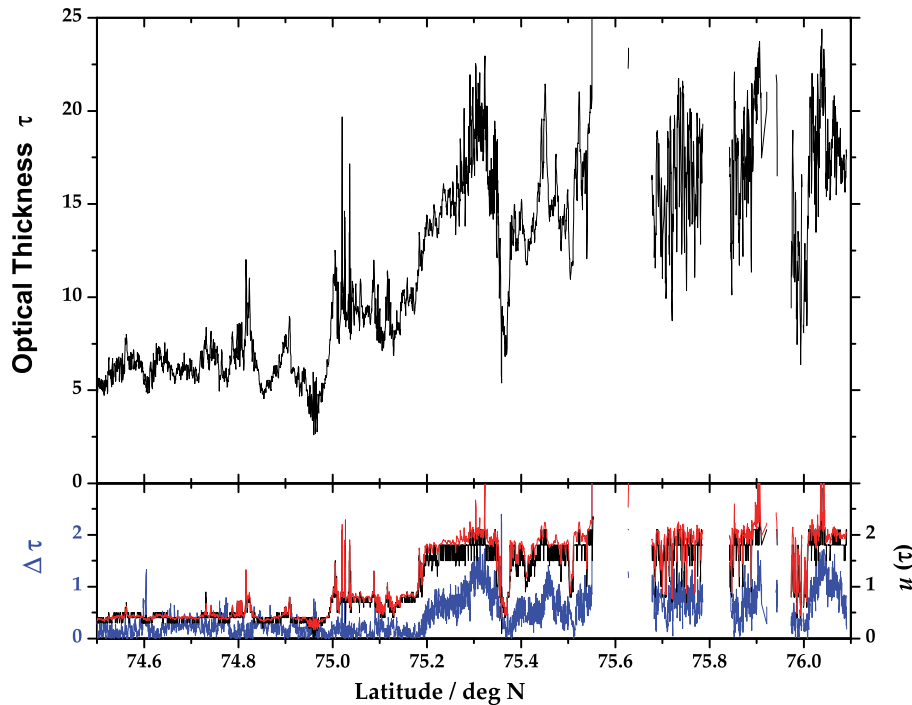
**Fig. 5.** Top panel: cloud optical thickness $\tau$ in aircraft nadir, retrieved from the SMART-Albedometer reflectance by 2WL. Bottom panel: absolute difference $\Delta\tau$ between $\tau$ retrieved by 2WL and 5WL (blue); propagated uncertainty $u(\tau)$ in 5WL (black) and 2WL (red).
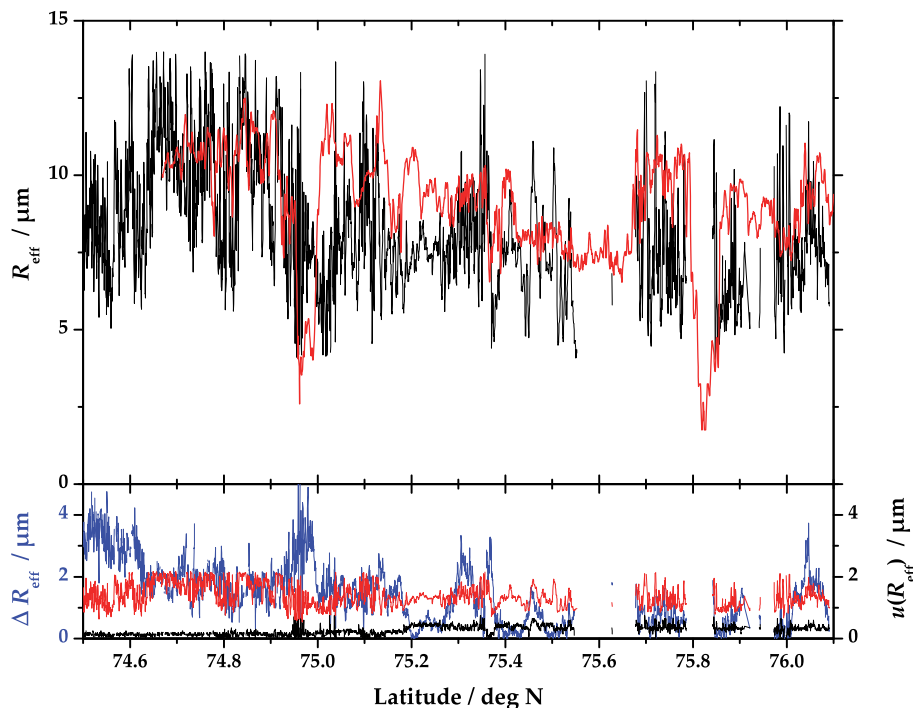
**Fig. 6.** Cloud-particle effective radius $r_{eff}$ in aircraft nadir, retrieved from the SMART-Albedometer reflectance. Top panel: $r_{eff}$ retrieved by 2WL (black) and observed by the FSSP (red) at the same latitude, but 1 h later. Bottom panel: absolute difference $\Delta r_{eff}$ between 2WL and 5WL (blue); propagated uncertainty $u(r_{eff})$ in 5WL (black) and 2WL (red).
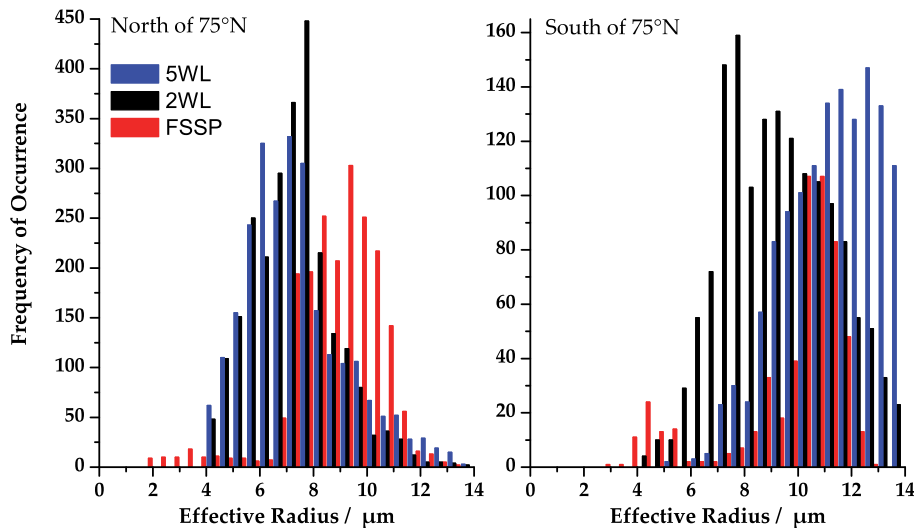
**Fig. 7.** Histograms showing the effective radius, retrieved from the SMART-Albedometer reflectance by 5WL (blue) and 2WL (black) and as observed by the FSSP (red) at the same latitude, but one hour later. Left: for the flight section north of 75° N. Right: South of 75° N.
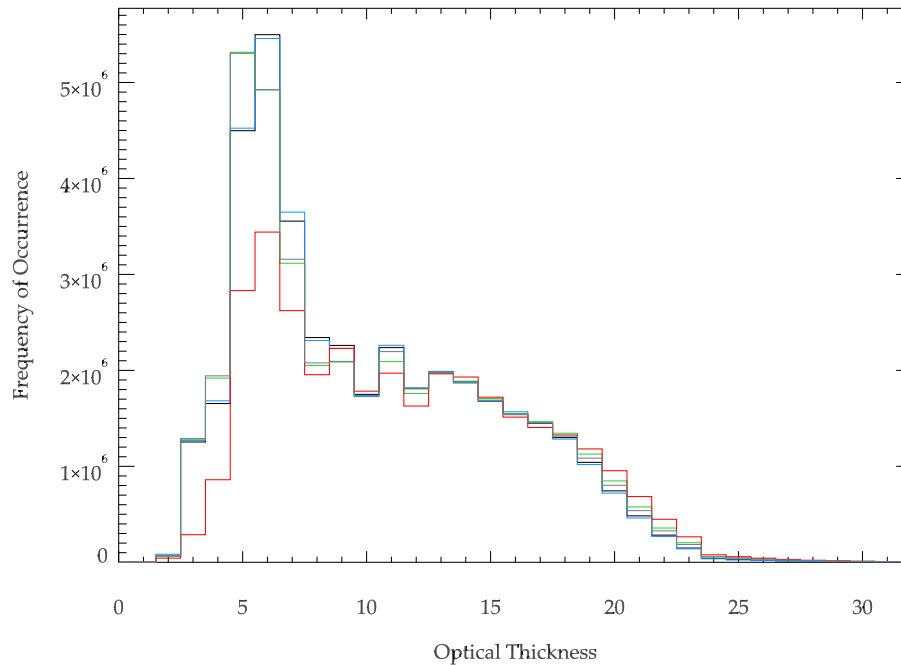
**Fig. 8.** Histogram of the optical thickness retrieved with different constraints of the effective radius. (1) black, (2) blue, (3) green, (4) red, (5) grey.
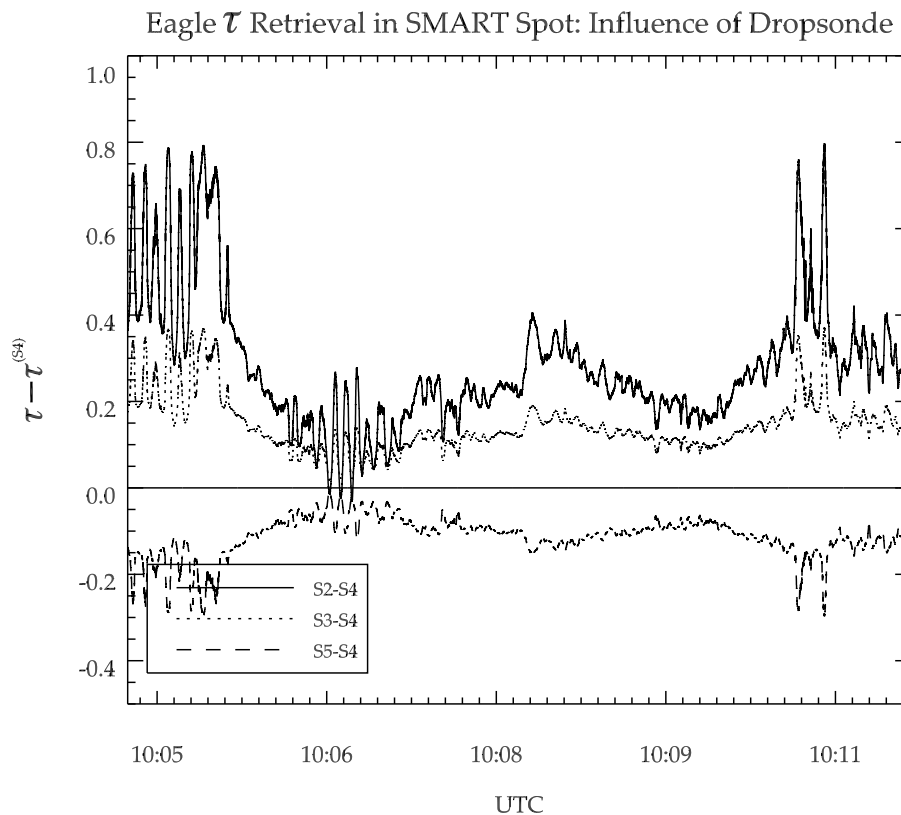
**Fig. 9.** Influence of the atmospheric profile used in the creation of the look-up tables.
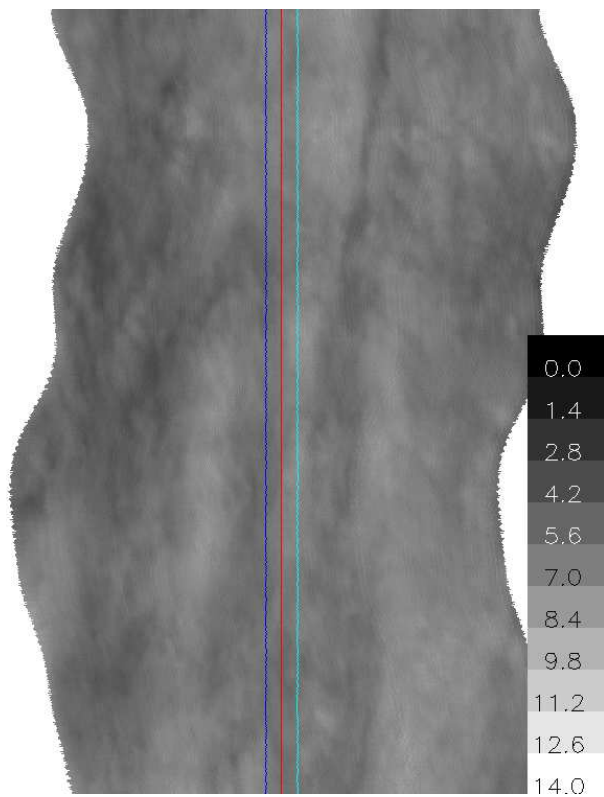
**Fig. 10.** Map of the cloud optical thickness, retrieved from hyperspectral radiance measurements by the AisaEAGLE on 17 May 2010 at 10:14 UTC. The red curve shows true nadir, the blue lines delineate the field of view of the SMART-Albedometer radiance.
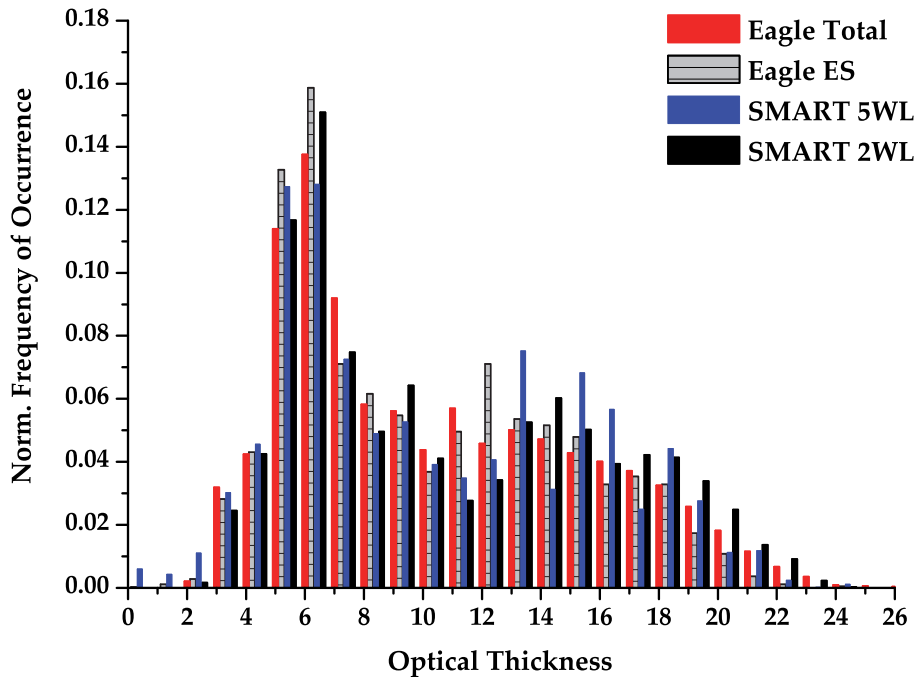
**Fig. 11.** Histogram of the cloud optical thickness retrieved from the hyperspectral radiances in all pixels (red) and in the nadir (ES) pixels (gray); and from the SMART-Albedometer nadir radiances (5WL algorithm in blue, 2WL in black).
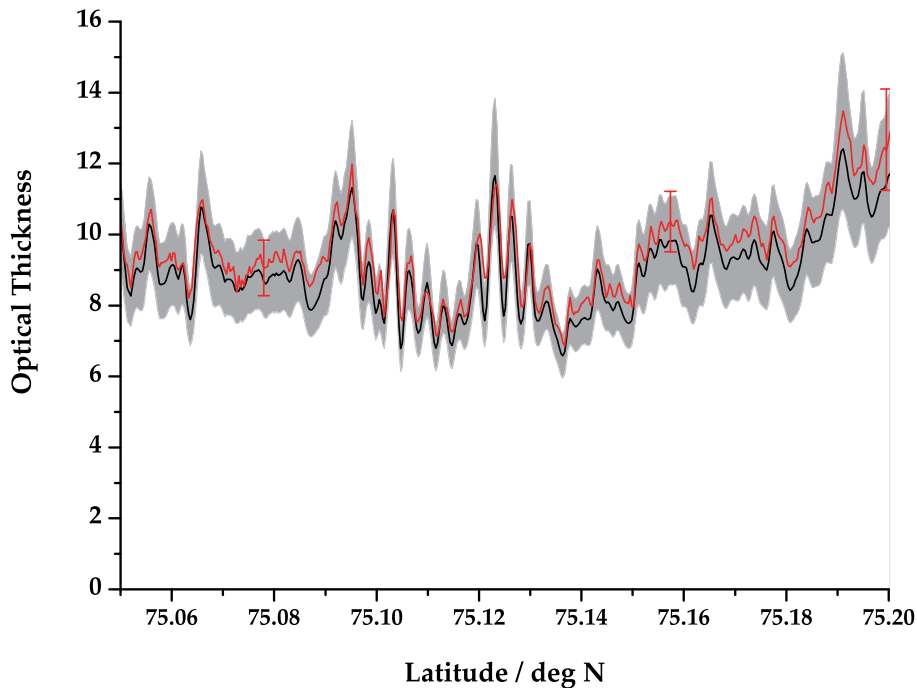
**Fig. 12.** Time series (excerpt) of the average cloud optical thickness in the ES pixels of the AisaEAGLE (black, with uncertainty range in grey), compared to that retrieved from the SMART-Albedometer radiance (red, with uncertainty range indicated by exemplary error bars).